npj | 2D materials and applications

www.nature.com/npj2dmaterials

ARTICLE OPEN

High-refractive index and mechanically cleavable non-van der Waals $InGaS_3$

Adilet N. Toksumakov[1,2,9], Georgy A. Ermolaev[1,9], Aleksandr S. Slavich[1], Natalia V. Doroshina[1], Ekaterina V. Sukhanova[2], Dmitry I. Yakubovsky[1], Alexander V. Syuy[1], Sergey M. Novikov[1], Roman I. Romanov[3], Andrey M. Markeev[4], Aleksandr S. Oreshonkov[5,6], Dmitry M. Tsymbarenko[7], Zakhar I. Popov[2], Dmitry G. Kvashnin[2], Andrey A. Vyshnevyy[1], Aleksey V. Arsenin[1,8], Davit A. Ghazaryan[1]✉ and Valentyn S. Volkov[1,8]✉

The growing family of two-dimensional crystals has been recognized as a promising platform for investigation of rich low-dimension physics and production of a variety of devices. Of particular interest are recently reported atomic sheets of non-van der Waals materials, which reshape our understanding of chemical bonds and enable heterostructures with novel functionality. Here, we study the structural and optical properties of ultrathin non-van der Waals $InGaS_3$ sheets produced by standard mechanical cleavage. Our ab initio calculations reveal weak out-of-plane covalent bonds, responsible for the layered structure of the material. The energy required for isolation of a single layer is as low as ~50 meVÅ^{-2}, which is comparable with the conventional van der Waals material's monolayer isolation energies of 20–60 meVÅ^{-2}. A comprehensive study of the structural, vibrational, and optical properties of the material reveals its wide bandgap (2.73 eV), high refractive index (>2.5) and negligible losses in the visible and infrared spectral ranges. These properties make it a perfect candidate for visible-range all-dielectric nanophotonics.

npj 2D Materials and Applications (2022)6:85 ; https://doi.org/10.1038/s41699-022-00359-9

INTRODUCTION

Layered materials with weak out-of-plane van der Waals bonds attract great research interest. These materials are studied in natural[1,2] and artificial formations[3–6]. Based on the stoichiometric composition and crystal structure, one can classify the natural van der Waals materials into graphene, transition metal dichalcogenide or mono-chalcogenide, sulfosalt, oxide, neo-, phyllosilicate and phosphate families. Artificial heterostructures are assembled by stacking atomic layers of van der Waals materials on top of each other[3,7]. Alternatively, one can categorise layered materials based on the feasibility of their exfoliation into separate atomic sheets[8], with its quantitative measure being an energy required for the isolation or separation of a singular atomic layer from the bulk[9,10]. In first principles calculations, the isolation energy can be estimated by evaluation of the interlayer binding energy per unit area. Within this approach, it is reasonable to distinguish naturally, potentially cleavable, and robust materials with threshold exfoliation energies of the order of[8] 10 meVÅ^{-2}, 100 meVÅ^{-2}, and 1000 meVÅ^{-2}, respectively. Apart from natural van der Waals formations, some of the cleavable materials have no van der Waals bonds in their structure. They form interlayer bonds of a different nature, *e.g.*, covalent, but of comparable strengths and bear the name of non-van der Waals materials[11–18]. Vivid examples are atomic sheets of Fe_2O_3[15], $AgCrS_2$[16] and FeS_2[19] obtained *via* sonication-assisted and cation-intercalation exfoliation methods, respectively.

In this article, we explore the structural and optical properties of the hexagonal phase of $InGaS_3$ thereby expanding the list of non-van der Waals materials. Contrary to the previous theoretical work, which predicts that $InGaS_3$ has an orthorhombic crystal structure with well-defined atomic layers connected by van der Waals bonds[20], we find that our samples have a hexagonal crystal structure with no van der Waals bonds in the unit cell. Surprisingly, those can be cleaved down to atomically thin sheets owing to the weak out-of-plane non-van der Waals bonds. We confirm the crystal structure by X-ray crystallography and discover the weak bonds by first-principles calculations. In addition, we study the optical properties both experimentally by imaging spectroscopic ellipsometry and theoretically by first principles calculations. Ab initio calculations are performed for orthorhombic and hexagonal phases, with only the latter agreeing with the experiment. As a result, we conclude that the hexagonal $InGaS_3$ is a wide bandgap (2.73 eV) cleavable semiconductor with high-refractive index (>2.5) and negligible optical losses in the visible and near-infrared spectral ranges, which makes it a unique material for the visible range nanophotonics and Mie-tronics.

RESULTS

Structure and morphology of non-van der Waals $InGaS_3$

Typical $InGaS_3$ crystals appear with yellow-to-lustrous grey shades as displayed in Fig. 1 (a). Such colours are determined by the 1:1:3 ratio distribution of Indium: Gallium: Sulphur atoms (see EDX and XPS spectroscopy patterns in Supplementary Figure 1). The crystals exhibit a hexagonal arrangement of III-III-VI group elements in the $P6_5$ space group with lattice parameters of $a = b = 6.6$ Å and $c = 17.9$ Å as presented in the inset of Fig. 1 (a). Our crystallographic imaging results confirm its hexagonal

[1]Center for Photonics and 2D Materials, Moscow Institute of Physics and Technology, Dolgoprudny 141700, Russia. [2]Emanuel Institute of Biochemical Physics RAS, Moscow 119334, Russia. [3]National Research Nuclear University MEPhI (Moscow Engineering Physics Institute), Moscow 115409, Russia. [4]Moscow Institute of Physics and Technology, Dolgoprudny 141701, Russia. [5]School of Engineering and Construction, Siberian Federal University, Krasnoyarsk 660041, Russia. [6]Laboratory of Molecular Spectroscopy, Kirensky Institute of Physics, Federal Research Center KSC SB RAS, Krasnoyarsk 660036, Russia. [7]Department of Chemistry, Lomonosov Moscow State University, Moscow 119991, Russia. [8]XPANCEO, Moscow 127495, Russia. [9]These authors contributed equally: Adilet N. Toksumakov, Georgy A. Ermolaev.
✉email: dav280892@gmail.com; vsv.mipt@gmail.com

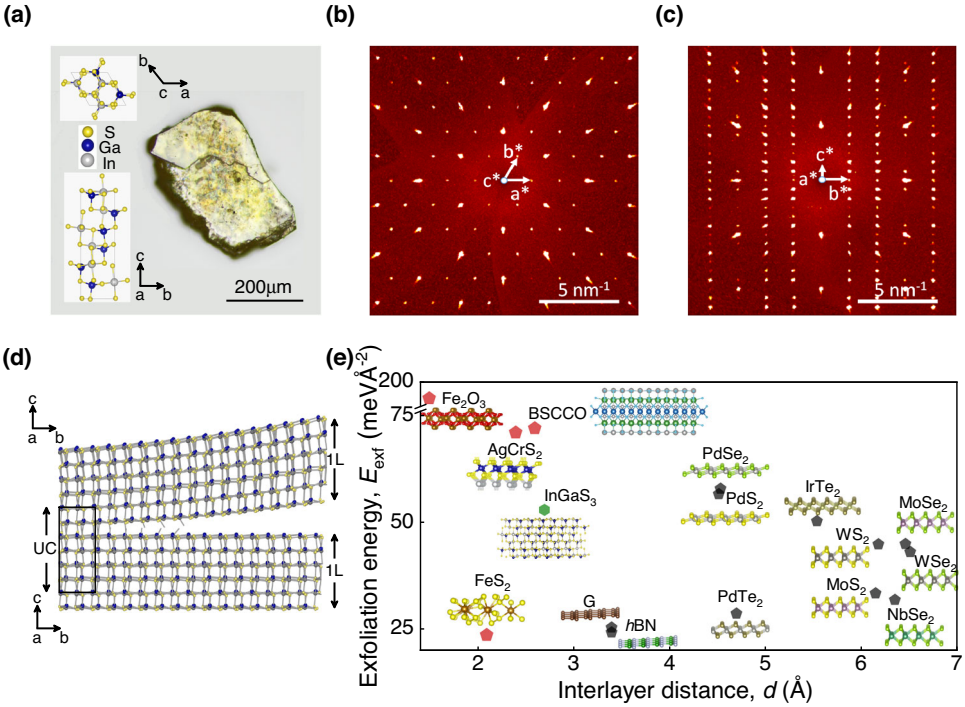

Fig. 1 Crystal structure and interlayer binding energies of non-van der Waals $InGaS_3$. a 5X optical micrograph of bulk crystal on a glass slide. Inset: Top and side views of $P6_5$ space group hexagonal crystal structure with lattice constants of $a = b = 6.6$ Å, $c = 17.9$ Å. *a*, *b*, *c* and *a**, *b**, *c** label real and reciprocal space crystallographic axes, correspondingly. **b** X-ray diffraction micrograph of the crystal presented in panel (**a**) across *a*b**-plane. **c** Same as (**b**), but across *c*b**-plane. **d** Schematic illustration of layer separation achieved by cutting off the weak non-van der Waals bonds. UC, 1 L stand for unit cell and cleaved monolayer, respectively. **e** Typical exfoliation energies of conventional van der Waals (black pentagons) and non-van der Waals (red pentagons) materials evaluated *via* first principles calculations. Green hexagon presents our estimation of the exfoliation energy along the proposed minimal energy atomic plane.

structure. It was refined in a chiral $P6_5$ space group giving an appropriate value of Flack's parameter of 0.06(2) being close to zero. Figure 1 (b, c) demonstrates the selected X-ray diffraction patterns across *a*b** and *c*b** crystallographic planes. Notably, a similar hexagonal structure of $InGaS_3$ was previously reported with a high *R*-value, 8.1 %, in the chiral $P6_1$ space group[21]. However, testing the space group for the dataset collected from our samples resulted in an unsatisfactory Flack's parameter of 0.94(3) which is in support of a swap within an enantiomorphic pair, $P6_1$ -> $P6_5$[22]. Further details on data collection, refinement parameters and interatomic distances are provided in Methods and Supplementary Tables 1 and 2. The hexagonal structure of the studied material was alternatively verified through transmission electron microscopy (see Supplementary Figure 2 for diffraction pattern across *a*b** crystallographic plane reflex interpretations).

The hexagonal $InGaS_3$ contains various structural bonds, whose strengths were estimated by first-principles calculations based on the density functional theory (DFT). To obtain isolation energy of individual atomic sheets, we estimated the difference between the ground-state energy of the relaxed structure and all of its unrelaxed substructures. Afterwards, we looked for the planes with the minimal binding energies to determine potentially breakable, or, in our case, cleavable directions. Excluding the relaxation energy of substructures, we found the exfoliation energy of $E_{exf} \approx 53$ meVÅ^{-2} for the plane shown in Fig. 1d. Notably, the exfoliation energy decreased when we added more atomic layers into our model. In the case of five layers, we obtained $E_{exf} = 47$ meV/Å^{-2}. After accounting for the further relaxation of the isolated layers[23], we obtained an even smaller value of $E^*_{exf} \approx 21$ meVÅ^{-2}. It is important to note, that some alternative and DFT accuracy approaches, such as MLIP provide computationally faster studies of mechanical properties of materials under the external deformations including exfoliation effects[24,25]. Figure 1e compares our results with the evaluated exfoliation energies of conventional van der Waals (and non-van der Waals) materials. Notably, the energies of conventional van der Waals materials cover the range of 20 to 60 meVÅ^{-2}, whereas non-van der Waals materials fall into a broader range from 25 to 180 meVÅ^{-2}. Among non-van der Waals materials, $InGaS_3$ has a relatively low exfoliation energy, which is even lower than that of some van der Waals materials, such as PdS_2 and $PdSe_2$.

Slightly elevated temperature treatment within the standard exfoliation procedure (see Methods)[7] allows for the cleavage of $InGaS_3$ crystals into individual nanosheets with atomically smooth surfaces (see Fig. 2a). However, ultrathin flakes are often highly inhomogeneous or cracked (see Supplementary Figure 3 for the atomic-force micrographs of inhomogeneous atomic sheets). This can be attributed to the lack of strength of some in-plane bonds within the material, leading to their random breakage during exfoliation. Figure 2b–d show AFM scans of pristine atomic sheets with nearly atomically flat surfaces (root-mean-square roughness of 0.3 nm). Thicknesses of these sheets correspond to one (1 L), two (2 L), three (3 L), four (4 L) and five (5 L) monolayers.

Figure 2f shows Raman spectra of the hexagonal $InGaS_3$ nanosheets taken at room and liquid nitrogen temperatures. Obtained spectral profiles have a complex form due to the overlapping bands, although peaks are slightly sharper at lower temperatures. The profiles display depths at wavenumber ranges of 180–200 cm^{-1} and 270–290 cm^{-1}, which is in good agreement with our lattice dynamics calculations (see vertical bars on the inset of Fig. 2f). Those predict an absence of vibrational modes within these wavenumber ranges (see Methods for calculation details). For hexagonal $InGaS_3$ in the $P6_5$ space group, we found 90 normal vibrational modes in the centre of the first Brillouin zone. Those can be represented by the expression $\Gamma_v = 15A + 15B + 15E_1 + 15E_2$. Here, $A + E_1$ are acoustical translational modes, *B* are

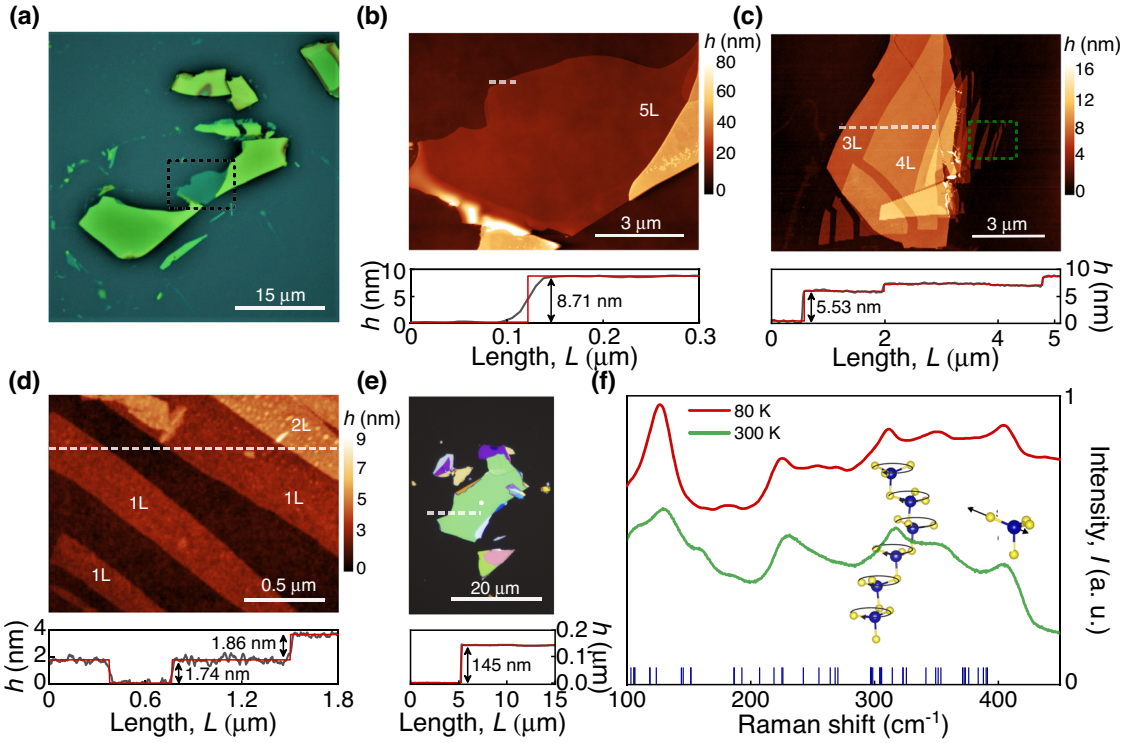

Fig. 2 Cleavage feasibility of non-van der Waals $InGaS_3$. a 100X optical micrograph of a typical nanosheet on Si/SiO_2 substrate. **b** AFM topographical scan over the region marked by dashed rectangle in panel (**a**). Height profile is taken along the dashed line in the map, showing the thickness equivalent to 5 L (8.71 ± 0.38 nm). **c** Same as in panel (**b**), but for thinner atomic sheets, with a thickness equivalent to 3 L (5.53 ± 0.32 nm) and 4 L (7.3 ± 0.34 nm). **d** Same as in panel (**c**), but for a magnified region marked by the dashed rectangle in panel (**c**) showing atomic strips with thicknesses equivalent to 1 L (1.74 ± 0.24 nm) and 2 L (1.74 + 1.86 ± 0.28 nm). **e** 100X optical micrograph of a typical nanosheet on a quartz substrate. White dot marks the Raman spectra collection point (145 ± 4 nm). **f** Raman spectra of the nanosheet presented in panel (**e**) at room (green line) and liquid nitrogen (red line) temperatures. Vertical bars label evaluated Raman-active modes (see Supplementary Table 3 for details). Insets: Schematic representation of lattice vibration directions of the corresponding Raman-active modes.

the silent modes, $14A + 14E_1$ are infrared-active modes, while $14A + 14E_1 + 15E_2$ are Raman-active modes. Their wavenumbers at zero pressure are presented in Supplementary Table 3. The contribution of individual atoms to the vibrational modes, *i.e.*, the partial phonon density of states (pPDoS), is depicted in Supplementary Figure 4. According to our pPDoS evaluations, the strong peak at 125 cm^{-1} is a mixed vibration of Gallium and Indium atoms, while the weak shoulder at the low-wavenumber region (157 cm^{-1}) is related to Gallium translations. The middle range of the spectra (from 200 to 270 cm^{-1}) associates with Sulphur vibrations. The high-wavenumber spectral part, above 290 cm^{-1}, mostly associates with Ga-S vibrations. An example of Gallium-Sulphur stretching-like mode is shown in Fig. 2 (f, right inset). Tetrahedral GaS_4 complexes combined in chains connected by common Sulphur atoms are capable of specific rotational vibrations, such as those demonstrated in Fig. 2 (f, mid inset). In this case, the rotation of triangle-like GaS_3 units is observed. Raman spectra of thinner, up to bilayer, sheets are shown in Supplementary Figure 5. They exhibit no apparent shift in the peak positions and an expected decline in the peak amplitudes.

Anisotropic optical properties and crystal structure reckoning of non-van der Waals $InGaS_3$

We investigated the anisotropic dielectric tensor (Fig. 3a) of hexagonal $InGaS_3$ through imaging spectroscopic ellipsometry in the tiny region of interest of 10 μm^2 within the area of exfoliated sheets. The ability to focus on the homogeneous high-quality region is a key benefit of our imaging technology[26]. Furthermore, we simultaneously recorded and analysed optical response from four $InGaS_3$ sheets to ensure a great precision and reproducibility of our results (see Methods and Supplementary Information for details). The dielectric function of hexagonal $InGaS_3$, similarly to transition metal dichalcogenides, is best represented by the Tauc-Lorentz oscillators[27,28] and the Cauchy model[29] across the crystallographic *ab*-plane and *c*-axis, respectively. Despite this, owing to the high thickness of monolayers and the non-van der Waals interaction in $InGaS_3$, the measured birefringence is relatively weak with $\Delta n \sim 0.1$ (the inset in Fig. 3a), contrasting the huge anisotropy of $\Delta n \sim 1.5$ in transition metal dichalcogenides with natural van der Waals bonds[26]. To explain this relatively weak anisotropy, we have performed additional DFT calculations (see Fig. 3b). The comparison of plots in Fig. 3a, b reveals a good agreement between experimental and theoretical results. Furthermore, our evaluations independently confirm the crystal structure of $InGaS_3$ (see inset of Fig. 1a) since the dielectric response is a fingerprint of the material's electronic bandstructure (see Supplementary Information for details). We also evaluated optical constants for the orthorhombic phase of $InGaS_3$ predicted theoretically in recent work[20]. The obtained constants, presented in Supplementary Figure 7, clearly disagree with our experimental results, which indirectly indicates the hexagonal crystal structure of our sample.

Additionally, a good agreement between experimental and theoretical optical responses (see Fig. 3) implicitly shows a small influence of spin-orbit coupling (SOC) in contrast to transition metal dichalcogenides,[24] where SOC leads to noticeable mismatch between DFT and experimental results. Hence, our technique, which combines a spectroscopic ellipsometry with density functional calculations unambiguously confirms the hexagonal structure of $InGaS_3$ in addition to the X-ray analysis and can be

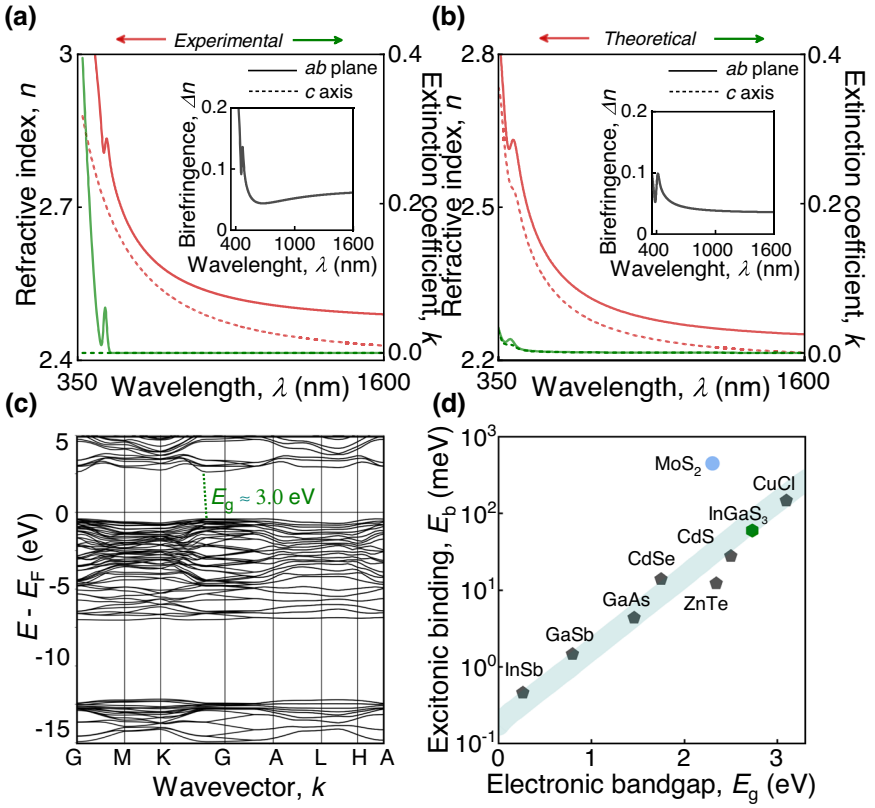

Fig. 3 Optical response of non-van der Waals $InGaS_3$. a Experimental and **b** first-principle refractive indices and extinction coefficients for *ab*-plane (straight line) and *c*-axis (dashed line) of commensurate values and trends validating the hexagonal structure of $InGaS_3$ (see Fig. 1(a (inset) and d)). Insets: material's birefringence. **c** Electronic bandstructure from the first-principle calculations. Fermi energy (E_F) is shifted to zero for clarity. Electronic bandgap is of $E_g = 3$ eV. **d** Excitonic binding energy versus electronic bandgap in traditional semiconductor materials. For a comparison, we also included the corresponding data for MoS_2 monolayer[55].

potentially used for the identification of crystal structures of other materials.

Apart from optical constants, we also evaluated the electronic bandstructure of hexagonal $InGaS_3$ (Fig. 3c) and individual orbital-resolved density of electronic states (see Supplementary Figure 6) using the Heyd-Scuseria-Ernzerhof hybrid functional (see Methods)[30]. For the latter, the main contributions to the bottom of conduction bands come from *s*-states of Gallium, Indium, and *p*-states of Sulphur atoms. From Fig. 3c, we conclude that $InGaS_3$ is an indirect bandgap semiconductor with $E_g = 3.0$ eV, which is close to bandgap ($E_g = 2.73$ eV) obtained experimentally from ellipsometry analysis. Moreover, we observed an excitonic peak at $E_{exc} = 2.67$ eV (464 nm) in optical response of the material, which is shown in Fig. 3a.

Its excitonic binding energy is $E_b = E_g - E_{exc} = 60$ meV. Interestingly, these values ($E_g = 2.73$ eV and $E_b = 60$ meV) are in line with bandgaps and excitonic binding energies of traditional semiconductors but contrast with transition metal dichalcogenides, such as MoS_2 (Fig. 3d). We believe it results from two main reasons: (*i*) the unit cell along the crystallographic *c*-axis of $InGaS_3$ is about 3 times larger than for MoS_2; (*ii*) $InGaS_3$ refractive index is about 2 times smaller compared to MoS_2. Hence, we estimate that $InGaS_3$ should have much weaker quantum confinement making it closer to 3D rather than 2D materials. Therefore, $InGaS_3$ does not exhibit extraordinary excitonic effects and birefringence as MoS_2. This indicates that the exciton in $InGaS_3$ has the same physical origin as in traditional semiconductors, and thus, can be described by the Wannier-Mott model[31].

Finally, we would like to highlight the strong dielectric response of $InGaS_3$ (Fig. 4a). Its refractive index is comparable to indices of classical high-index materials, such as silicon (Si)[32] and titanium oxide (TiO_2)[33,34], as well as emerging high-index materials, such as Gallium Phosphide (GaP)[35] and tin(IV) Sulphide (SnS_2)[36], as shown in Fig. 4a. More importantly, $InGaS_3$ has zero optical losses up to 2.57 eV (485 nm), as can be seen in Fig. 4b. This value lies between optical bandgaps of SnS_2 ($E_g = 2.18$ eV) and TiO_2 ($E_g = 3.35$ eV). Hence, $InGaS_3$ covers an important gap in visible spectral range for high-refractive index materials (see inset in Fig. 4b). As a result, we conclude that it is an outstanding material for the novel research direction of all-dielectric meta-optics in the visible range[35,37]. To demonstrate that $InGaS_3$ outperforms other transparent materials in the visible range, we have studied planar waveguides on a quartz substrate. Setting the operating free space wavelength to 500 nm, we find (Fig. 4c) that $InGaS_3$ allows for a much stronger field confinement of $\lambda/9$ than TiO_2 ($\lambda/5.6$) and with the much thinner core layer (32 nm *vs* 57 nm). These results are surprising in light of a relatively small refractive index difference of about 18% between $InGaS_3$ and TiO_2 at 500 nm. Although $InGaS_3$ and TiO_2 waveguides are both very small, mode length evaluated here governs the Purcell enhancement of spontaneous emission[38]. As a result, single-photon sources and nanoLEDs coupled to $InGaS_3$ waveguides would have higher internal quantum efficiency and their radiation would be better collected by the waveguide.

DISCUSSION

To sum up, we have demonstrated that hexagonal $InGaS_3$ can be cleaved down to thicknesses of individual monolayers even though it is not composed of atomic layers connected by van der Waals bonds within its unit cell. It is made possible due to a specific arrangement of atoms across the crystallographic *c*-axis, where the exfoliation energy diminishes to 53 meVÅ^{-2} for a

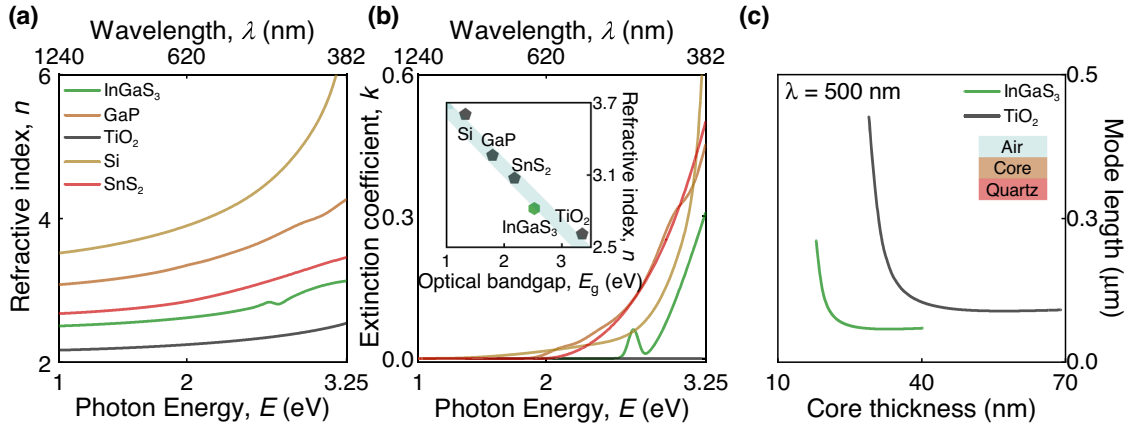

Fig. 4 Towards visible-range all-dielectric nanophotonics with non-van der Waals $InGaS_3$. a Refractive index and **b** extinction coefficient spectra of visible-range high-refractive index and low-loss materials. Inset: The correlation between refractive indices and optical bandgaps for high-refractive index materials. **c** Plots of the mode length of the fundamental mode as a function of core thickness in a planar nanophotonic waveguide with $InGaS_3$ and TiO_2 as core materials.

selected atomic plane. This exfoliation energy value is comparable to conventional van der Waals materials. Furthermore, the hexagonal $InGaS_3$ is well suited for next-generation nanophotonics, Mie-tronics[39], and expands high-refractive index pallette[40]. In particular, it meets two major requirements of Mie-tronics: high-refractive index ($n > 2.5$) and broadband transparency ($k \approx 0$ above 465 nm). Although, its refractive index is only about ~18 % higher than of traditional TiO_2[41], we show that $InGaS_3$ planar waveguides have by 55 % stronger field confinement achieved at 40 % lower thickness than TiO_2 waveguides. Hence, we expect that all-dielectric nanostructures, such as waveguides[42], Mie-resonance nanoparticles[43], and subwavelength metasurfaces[44] based on $InGaS_3$ would benefit greatly from its higher refractive index. Additionally, it exhibits an out-of-plane optical anisotropy ($\Delta n \sim 0.1$), in contrast to conventional high-refractive index materials, which may greatly extend its scope of applications. Therefore, $InGaS_3$ possesses a unique combination of optical properties, such as high-refractive index, zero optical losses and out-of-plane anisotropy also offering convenient thickness control due to its structural properties.

METHODS

Sample preparation

Bulk $InGaS_3$ crystals were purchased from 2D Semiconductors (Scottsdale, USA) and exfoliated on top of required substrates: Si/SiO_2 and quartz. Prior to exfoliation, the corresponding substrates were subsequently cleaned in acetone, isopropanol alcohol, and deionized water. Then, those were subjected to oxygen plasma (O_2) to remove the ambient adsorbates. Following the plasma cleaning, substrates were put on a hot plate at the temperatures of 120–140 °C for 2 min. After the heating, the scotch-tape from Nitto Denko Corporation (Osaka, Japan) with loaded crustal $InGaS_3$ was brought in contact with substrates. Afterwards, the tape was removed completing the exfoliation procedure.

X-ray crystallography

X-ray diffraction analysis of $InGaS_3$ single crystals was performed on Bruker D8 QUEST diffractometer with Photon III CMOS detector using Mo Kα radiation ($l = 0.71073$ Å) focused by multilayer Montel mirror. The full dataset was collected at the temperature of 100 K within ω-scans indexed with cell-now. It was integrated through SAINT from the SHELXTL PLUS package[45]. Absorption correction was completed by a multiscan approach implemented from SADABS[46]. The crystal structure was solved by direct methods and refined anisotropically with full-matrix F^2 least-squares technique using SHELXTL PLUS package. The structure was refined in a chiral $P6_5$ space group with the resulting Flack parameter of 0.06 (2) being close to zero[47]. The second virtual inversion twin-component was added to refinement by TWIN/BASF instruction to account for the absolute structural parameter. This led to a slight reduction of R-value from 2.50 to 2.49%.

Density functional theory

Calculations of electronic bandstructure and optical constants were performed using the Vienna ab-initio simulation package VASP[48,49] within generalized gradient approximation (GGA)[50]. The Heyd-Scuseria-Ernzerhof (HSE) hybrid functional[51] in combination with Perdew-Burke-Ernzerhof (PBE)[52] potentials was applied for accurate description of the electronic bandstructure. Electron-ion interactions were described by projector-augmented wave (PAW) method[52,53]. The cutoff energy for the plane-wave basis was set to 400 eV. The first Brillouin zone of the supercells was sampled with a $6 \times 6 \times 3$ Monkhorst-Pack mesh[54] of k-points for bulk supercell and $6 \times 6 \times 1$ for monolayer case. The maximal force convergence tolerance settings for geometry optimization were set to 0.01 eVÅ^{-1}.

Lattice dynamics calculations

First-principle lattice dynamics calculations were carried out with the CASTEP code package[55]. The crystal structure was fully optimized using LD approximation with CA-PZ exchange-correlation functional based on Ceperley and Alder numerical representation[56] parameterized by Perdew and Zunger[57]. Maximal force and stress tensor convergence tolerance settings for geometry optimization were set to 0.01 eVÅ^{-1} and 0.02 GPa, respectively. $5s_2$ $5p_1$, $3d_{10}$ $4s_2$ $4p_1$, and $3s_2$ $3p_4$ orbitals were considered occupied with valence electrons for Indium, Gallium and Sulphur, respectively. Plane-wave cutoff energy was set to 880 eV for $4 \times 4 \times 2$ sampling of the first Brillouin zone by the Monkhorst-Pack method.

Atomic Force Microscopy

The thickness and surface morphology of $InGaS_3$ sheets were accurately characterized by an atomic force microscope (NT-MDT Ntegra II) operated in a HybriD mode at ambient conditions. AFM images were acquired using silicon tips from TipsNano (GOLDEN, NSG 10) with spring constant of 11.8 N/m, head curvature radius <10 nm, and resonant frequency of 240 kHz. The measurements

were performed at a scan rate of 0.3 Hz and 512-pixel resolution. The obtained datasets were analysed by the Gwyddion software.

Imaging spectroscopic ellipsometry

To analyze anisotropic optical response of $InGaS_3$, we used commercial imaging spectroscopic ellipsometer Accurion nanofilm_ep4 in the nulling mode. Ellipsometry spectra were recorded for four sheets with various thicknesses ($h = 3.6$ nm, 68.5 nm, 103.0 nm, and 277.4 nm) in the spectral range from ultraviolet (360 nm) to near infrared (1700 nm). For ellipsometry analysis, we followed the algorithm described in Supplementary Note 2 of our recent work[26].

Eigenmode simulations

To study planar photonic waveguides with anisotropic $InGaS_3$ and isotropic TiO_2 cores, we employed a finite element method solver implemented in COMSOL Multiphysics software. The mode length was evaluated as:

$$I_{mode} = \frac{\int_{-\infty}^{\infty} W_{em} dy}{max(W_{em})} \quad (1)$$

where

$$W_{em} = \frac{1}{16\pi}\left[\frac{\partial(\omega\varepsilon)}{\partial\omega}|E|^2 + |H|^2\right] \quad (2)$$

is the electromagnetic energy density in dispersive non-magnetic media.

DATA AVAILABILITY

The data that support the plots and other findings of this study are available from the corresponding authors upon reasonable request. The X-ray crystallographic coordinates for the structure reported in this study have been deposited at the Cambridge Crystallographic Data Centre (CCDC), under deposition number 2145523. It can be obtained free of charge from The Cambridge Crystallographic Data Centre *via* www.ccdc.cam.ac.uk/data_request/cif.

Received: 5 May 2022; Accepted: 3 November 2022;
Published online: 24 November 2022

REFERENCES

1. Frisenda R, Niu Y, Gant P, Muñoz M, Castellanos-Gomez A. Naturally occurring van der Waals materials. *npj 2D Materials and Applications*. **4**, (2020).
2. Velický, M. et al. Exfoliation of natural van der Waals heterostructures to a single unit cell thickness. *Nat. Commun.* **8**, 14410 (2017).
3. Geim, A. K. & Grigorieva, I. V. Van der Waals heterostructures. *Nature* **499**, 419–425 (2013).
4. 2D Materials and Van der Waals Heterostructures. MDPI Books. https://doi.org/10.3390/books978-3-03928-769-7.
5. Bonaccorso, F. et al. Graphene, related two-dimensional crystals, and hybrid systems for energy conversion and storage. *Science* **347**, 1246501 (2015).
6. Ferrari, A. C. et al. Science and technology roadmap for graphene, related two-dimensional crystals, and hybrid systems. *Nanoscale* **7**, 4598–4810 (2015).
7. Novoselov, K. S., Mishchenko, A., Carvalho, A. & Castro Neto, A. H. 2D materials and van der Waals heterostructures. *Science* **353**, aac9439 (2016).
8. Mounet, N. et al. Two-dimensional materials from high-throughput computational exfoliation of experimentally known compounds. *Nat. Nanotechnol.* **13**, 246–252 (2018).
9. Choudhary, K., Kalish, I., Beams, R. & Tavazza, F. High-throughput Identification and Characterization of Two-dimensional Materials using Density functional theory. *Sci. Rep.* **7**, 5179 (2017).
10. Björkman, T., Gulans, A., Krasheninnikov, A. V. & Nieminen, R. M. van der Waals bonding in layered compounds from advanced density-functional first-principles calculations. *Phys. Rev. Lett.* **108**, 235502 (2012).
11. Serles, P. et al. Friction of magnetene, a non–van der Waals 2D material. *Sci. Adv.* **7**, eabk2041 (2021).
12. Jin, C. & Kou, L. Two-dimensional non-van der Waals magnetic layers: functional materials for potential device applications. *J. Phys. D. Appl Phys.* **54**, 413001 (2021).
13. Puthirath Balan, A. et al. A Non-van der Waals Two-Dimensional Material from Natural Titanium Mineral Ore Ilmenite. *Chem. Mater.* **30**, 5923–5931 (2018).
14. Friedrich, R., Ghorbani-Asl, M., Curtarolo, S. & Krasheninnikov, A. V. Data-Driven Quest for Two-Dimensional Non-van der Waals Materials. *Nano Lett.* **22**, 989–997 (2022).
15. Puthirath Balan, A. et al. Exfoliation of a non-van der Waals material from iron ore hematite. *Nat. Nanotechnol.* **13**, 602–609 (2018).
16. Peng, J. et al. Stoichiometric two-dimensional non-van der Waals AgCrS2 with superionic behaviour at room temperature. *Nat. Chem.* **13**, 1235–1240 (2021).
17. Zhao SYF, et al. Sign-Reversing Hall Effect in Atomically Thin High-Temperature Bi2.1Sr1.9CaCu2.0O8 δ Superconductors. *Physical Review Letters*. **122**, (2019).
18. Bandyopadhyay, A., Frey, N. C., Jariwala, D. & Shenoy, V. B. Engineering Magnetic Phases in Two-Dimensional Non-van der Waals Transition-Metal Oxides. *Nano Lett.* **19**, 7793–7800 (2019).
19. Puthirath, A. B. et al. Apparent Ferromagnetism in Exfoliated Ultrathin Pyrite Sheets. *J. Phys. Chem. C.* **125**, 18927–18935 (2021).
20. Chen, W. et al. Anomalous layer-dependent electronic and piezoelectric properties of 2D GaInS3 nanosheets. *Appl Phys. Lett.* **118**, 213103 (2021).
21. *Inorganic Materials*. Consultants Bureau, 1987.
22. Flack, H. D. & Bernardinelli, G. The use of X-ray crystallography to determine absolute configuration. *Chirality* **20**, 681–690 (2008).
23. Jung, J. H., Park, C.-H. & Ihm, J. A Rigorous Method of Calculating Exfoliation Energies from First Principles. *Nano Lett.* **18**, 2759–2765 (2018).
24. Mortazavi, B. et al. First-Principles Multiscale Modeling of Mechanical Properties in Graphene/Borophene Heterostructures Empowered by Machine-Learning Interatomic Potentials. *Adv. Mater.* **33**, e2102807 (2021).
25. Mortazavi, B. et al. Exceptional piezoelectricity, high thermal conductivity and stiffness and promising photocatalysis in two-dimensional $MoSi_2N_4$ family confirmed by first-principles. *Nano Energy* **82**, 105716 (2021).
26. Ermolaev, G. A. et al. Giant optical anisotropy in transition metal dichalcogenides for next-generation photonics. *Nat. Commun.* **12**, 854 (2021).
27. Ermolaev, G. A., Yakubovsky, D. I., Stebunov, Y. V., Arsenin, A. V. & Volkov, V. S. Spectral ellipsometry of monolayer transition metal dichalcogenides: Analysis of excitonic peaks in dispersion. *J. Vac. Sci. Technol. B* **38**, 014002 (2020).
28. Ermolaev, G. et al. Topological phase singularities in atomically thin high-refractive-index materials. *Nat. Commun.* **13**, 2049 (2022).
29. Tompkins HG, Hilfiker JN. *Spectroscopic Ellipsometry: Practical Application to Thin Film Characterization*. 2015.
30. Heyd, J., Scuseria, G. E. & Ernzerhof, M. Hybrid functionals based on a screened Coulomb potential. The. *J. Chem. Phys.* **118**, 8207–8215 (2003).
31. Haug H, Koch SW. *Quantum Theory of the Optical and Electronic Properties of Semiconductors*. https://doi.org/10.1142/1977 (1993).
32. Herzinger, C. M., Johs, B., McGahan, W. A., Woollam, J. A. & Paulson, W. Ellipsometric determination of optical constants for silicon and thermally grown silicon dioxide via a multi-sample, multi-wavelength, multi-angle investigation. *J. Appl. Phys.* **83**, 3323–3336 (1998).
33. Tiwald TE, Schubert M. Measurement of rutile TiO_2 dielectric tensor from 0.148 to 33 μm using generalized ellipsometry. *SPIE Proceedings*. https://doi.org/10.1117/12.403587 (2000).
34. Ermolaev, E., Kushnir, S. & Napolskii Titania Photonic Crystals with Precise Photonic Band Gap Position via Anodizing with Voltage versus Optical Path Length Modulation. *Nanomaterials* **9**, 651 (2019).
35. Khmelevskaia, D. et al. Directly grown crystalline gallium phosphide on sapphire for nonlinear all-dielectric nanophotonics. *Appl. Phys. Lett.* **118**, 201101 (2021).
36. Ermolaev, G. A. et al. Broadband Optical Constants and Nonlinear Properties of SnS2 and SnSe2. *Nanomaterials* **12**, 141 (2021).
37. Kruk, S. & Kivshar, Y. Functional Meta-Optics and Nanophotonics Governed by Mie Resonances. *ACS Photonics* **4**, 2638–2649 (2017).
38. Vyshnevyy AA, Fedyanin DY. Hybrid Electro-Optical Pumping of Active Plasmonic Nanostructures. *Nanomaterials (Basel)* **10**, (2020).
39. Kivshar Y. The Rise of Mie-tronics. *Nano Lett* (2022).
40. Khurgin, J. B. Expanding the Photonic Palette: Exploring High Index Materials. *ACS Photonics* **9**, 743–751 (2022).
41. Dorrah, A. H., Rubin, N. A., Tamagnone, M., Zaidi, A. & Capasso, F. Structuring total angular momentum of light along the propagation direction with polarization-controlled meta-optics. *Nat. Commun.* **12**, 6249 (2021).
42. Hu, F. et al. Imaging exciton–polariton transport in $MoSe_2$ waveguides. *Nat. Photonics* **11**, 356–360 (2017).
43. Tselikov, Gl. et al. Transition metal dichalcogenide nanospheres for high-refractive-index nanophotonics and biomedical theranostics. *Proceedings of the National Academy of Sciences* **119**, e2208830119 (2022).
44. Dorrah, A. H. & Capasso, F. Tunable structured light with flat optics. *Science* **376**, eabi6860 (2022).
45. Sheldrick GM. SHELXTL v. 5.10, Structure Determination Software Suite, Bruker AXS, Madison (Wisconsin, USA). 1998.

46. Sheldrick GM. (1998a). SADABS v. 2.01, Bruker/Siemens Area Detector Absorption Correction Program, Bruker AXS, Madison, Wisconsin, USA. 1998.
47. Flack, H. D. & Bernardinelli, G. Absolute structure and absolute configuration. *Acta Crystallogr A* **55**, 908–915 (1999).
48. Kresse, G. & Furthmüller, J. Efficient iterative schemes for ab initio total-energy calculations using a plane-wave basis set. *Phys. Rev. B Condens Matter* **54**, 11169–11186 (1996).
49. Kresse, G. & Joubert, D. From ultrasoft pseudopotentials to the projector augmented-wave method. *Phys. Rev. B Condens Matter* **59**, 1758–1775 (1999).
50. Zhang, Y. & Yang, W. Comment on 'Generalized Gradient Approximation Made Simple'. *Phys. Rev. Lett.* **80**, 890–890 (1998).
51. Heyd, J. & Scuseria, G. E. Efficient hybrid density functional calculations in solids: Assessment of the Heyd–Scuseria–Ernzerhof screened Coulomb hybrid functional. *J. Chem. Phys.* **121**, 1187–1192 (2004).
52. Perdew, J. P., Burke, K. & Ernzerhof, M. Generalized Gradient Approximation Made Simple. *Phys. Rev. Lett.* **77**, 3865–3868 (1996).
53. Blöchl, P. E., Först, C. J. & Schimpl, J. Projector augmented wave method:ab initio molecular dynamics with full wave functions. *Bull. Mater. Sci.* **26**, 33–41 (2003).
54. Monkhorst, H. J. & Pack, J. D. Special points for Brillouin-zone integrations. *Phys. Rev. B Condens Matter* **13**, 5188–5192 (1976).
55. Clark, S. J. et al. First principles methods using CASTEP. *Z. f.ür. Kristallographie - Crystalline Mater.* **220**, 567–570 (2005).
56. Ceperley, D. M. & Alder, B. J. Ground State of the Electron Gas by a Stochastic Method. *Phys. Rev. Lett.* **45**, 566–569 (1980).
57. Perdew, J. P. & Zunger, A. Self-interaction correction to density-functional approximations for many-electron systems. *Phys. Rev. B Condens Matter* **23**, 5048–5079 (1981).

ACKNOWLEDGEMENTS

This work was supported by Russian Science Foundation project No. 21-79-00218 (experimental studies) and Ministry of Science and Higher Education of Russian Federation project No. 075-15-2021-606 (theoretical studies). The calculations were performed using the resources provided by to the Joint Supercomputer Center of the Russian Academy of Sciences. D.M.T. acknowledges the support from M.V. Lomonosov Moscow State University Program of Development.

AUTHOR CONTRIBUTIONS

D.A.G. and V.S.V. suggested and directed the project with help from A.V.A., A.N.T. fabricated the samples, G.A.E., A.S.S., N.V.D., D.I.Y., A.V.S., D.M.T., S.M.N., R.I.R., A.M.M. and D.A.G. performed the measurements and analysed the data, A.N.T., E.V.S., A.S.O., Z.I.P., D.G.K. and A.A.V. provided theoretical support. A.N.T., G.A.E., A.A.V., A.V.A., D.A.G., and V.S.V. contributed to the interpretation of experimental results. A.N.T. wrote the original draft with the help from G.A.E. D.A.G., A.A.V., A.V.A., and V.S.V. reviewed and edited the paper. All authors contributed to the discussions and commented on the paper.

COMPETING INTERESTS

The authors declare no competing interests.

ADDITIONAL INFORMATION

Supplementary information The online version contains supplementary material available at https://doi.org/10.1038/s41699-022-00359-9.

Correspondence and requests for materials should be addressed to Davit A. Ghazaryan or Valentyn S. Volkov.

Reprints and permission information is available at http://www.nature.com/reprints

Publisher's note Springer Nature remains neutral with regard to jurisdictional claims in published maps and institutional affiliations.